

# FeedbackSTS-Det: Sparse Frames-Based Spatio-Temporal Semantic Feedback Network for Infrared Small Target Detection

Yian Huang, *Student Member, IEEE*, Qing Qin\*, Aji Mao, Xiangyu Qiu, *Student Member, IEEE*, Liang Xu, Xian Zhang, Zhenming Peng\*, *Senior Member, IEEE*

**Abstract**—Infrared small target detection (ISTD) under complex backgrounds remains a critical yet challenging task, primarily due to the extremely low signal-to-clutter ratio, persistent dynamic interference, and the lack of distinct target features. While multi-frame detection methods leverages temporal cues to improve upon single-frame approaches, existing methods still struggle with inefficient long-range dependency modeling and insufficient robustness. To overcome these issues, we propose a novel scheme for ISTD, realized through a sparse frames-based spatio-temporal semantic feedback network named FeedbackSTS-Det. The core of our approach is a novel spatio-temporal semantic feedback strategy with a closed-loop semantic association mechanism, which consists of paired forward and backward refinement modules that work cooperatively across the encoder and decoder. Moreover, both modules incorporate an embedded sparse semantic module (SSM), which performs structured sparse temporal modeling to capture long-range dependencies with low computational cost. This integrated design facilitates robust implicit inter-frame registration and continuous semantic refinement, effectively suppressing false alarms. Furthermore, our overall procedure maintains a consistent training-inference pipeline, which ensures reliable performance transfer and increases model robustness. Extensive experiments on multiple benchmark datasets confirm the effectiveness of FeedbackSTS-Det. Code and models are available at: <https://github.com/IDIP-Lab/FeedbackSTS-Det>.

**Index Terms**—Infrared small target detection, sparse spatial-temporal semantics, feature alignment feedback, dynamic scenes.

## I. INTRODUCTION

INFRARED small target detection (ISTD) has served as a fundamental and critical technology over the past several decades, playing an essential role in both defense and civilian applications such as missile warning [1], [2], maritime surveillance [3], [4], and disaster monitoring [5]. Although traditional single-frame infrared small target (SIRST) detection methods have achieved notable progress, they suffer from an inherent limitation: the inability to leverage temporal motion cues, resulting in insufficient robustness under low signal-to-noise

This work was supported by the Natural Science Foundation of Sichuan Province of China (Grant No.2025ZNSFSC0522) and partially supported by the National Natural Science Foundation of China (Grant No.61571096). (Corresponding author: Zhenming Peng, Qing Qin).

Yian Huang, Aji Mao, Xiangyu Qiu, Liang Xu, Xian Zhang, and Zhenming Peng are with the School of Information and Communication Engineering and the Laboratory of Imaging Detection and Intelligent Perception, University of Electronic Science and Technology of China, Chengdu 611731, China (e-mail: huangyian1@std.uestc.edu.cn; ajimao@std.uestc.edu.cn; xiangyuqiu@std.uestc.edu.cn; liangx@std.uestc.edu.cn; zhangxian@std.uestc.edu.cn; zmpeng@uestc.edu.cn).

Qing Qin is with School of Television and Audiovisual Arts, Communication University of Zhejiang, Hangzhou 310018, China (e-mail: 20190012@cuz.edu.cn).

ratio (SNR) scenarios. To address this bottleneck, multi-frame infrared small target (MIRST) detection has emerged, which significantly enhances detection performance by integrating temporal contextual information.

Existing MIRST detection approaches can be broadly categorized into two technical paradigms. The first is model-driven methods, which rely on mathematical priors for target-background separation. Early filtering-based approaches [6], [7], and subsequent optimization-based methods leveraging low-rank and sparse decomposition [8], [9], [10] have demonstrated effectiveness in specific scenarios. More recent tensor-based extensions incorporate temporal information through spatio-temporal modeling [11], [12], [13]. Although theoretically principled, these methods often require meticulous manual tuning and struggle to adapt to complex, non-linear clutter environments.

The second category comprises data-driven methods that employ deep learning to automatically learn spatio-temporal features. These can be further divided into two implementation paradigms based on how temporal information is processed. The iterative feature propagation mode [14], [15], [16] processes sequences frame-by-frame, maintaining a hidden state that propagates temporal information forward. While computationally efficient, this approach suffers from error accumulation and training-inference inconsistency. Alternatively, the sliding-window mode [17], [18], [19] processes fixed-length frame segments, enabling more stable spatio-temporal integration at the cost of limited temporal receptive field and increased computational burden. Despite their advancements, both paradigms face persistent challenges:

In dense clutter environments, dim infrared small targets are strongly coupled with noise, background, and atmospheric interference, making signal separation difficult and leading to poor feature extraction accuracy, which severely hinders reliable detection. Additionally, the imaging scene often contains numerous false alarms, such as high-altitude cirrus clouds, thunderstorms, and forest fires, which form high-reflectance regions easily misclassified as targets, critically compromising discrimination performance. Moreover, the extremely small spatial extent of dim targets provides negligible shape or texture cues, particularly evident in high-altitude satellite imaging where targets often degrade into mere points, compelling reliance solely on their temporal radiation dynamics for detection.

To tackle these challenges, this paper proposes a novel sparse frames-based spatio-temporal semantic feedback semantics network, termed FeedbackSTS-Det. The core of our approach is a spatio-temporal semantic feedback strategy that establishes

a closed-loop semantic association mechanism. Specifically, it integrates a forward spatio-temporal semantic refinement module (FSTSRT) in the encoder and a backward spatio-temporal semantic refinement module (BSTSRT) in the decoder in a cooperative manner, both built upon a balanced 3D Res-UNet backbone. Additionally, we embed a sparse semantic module (SSM) within both refinement modules, which performs structured sparse temporal modeling to capture long-range dependencies with low computational cost. These designs facilitate robust implicit inter-frame registration and continuous spatio-temporal semantic refinement, ensuring effective false alarm suppression and consistent performance. Furthermore, our overall procedure maintains a consistent training-inference pipeline, which ensures reliable performance transfer and increases model robustness.

The main contributions of this work are summarized as follows:

- We propose a novel spatio-temporal semantic feedback strategy with a closed-loop semantic association mechanism for infrared small target detection. It consists of paired forward and backward refinement modules that work cooperatively across the encoder and decoder. This design facilitates robust implicit inter-frame registration and continuously refines spatio-temporal semantics to suppress false alarms from dynamic clutter.
- We introduce an embedded sparse semantic module (SSM), which operates by strategically grouping frames by interval, propagating semantics within each group, and reassembling the sequence to efficiently capture long-range temporal dependencies with low computational overhead, while inherently suppressing transient noise.
- Our overall procedure maintains a consistent training-inference pipeline, which ensures reliable performance transfer and increases model robustness.

The remainder of this paper is organized as follows: Section II provides a comprehensive review and critical analysis of related work. Section III describes the proposed network architecture. Section IV presents experimental results and analysis. Finally, Section V provides concluding remarks.

## II. RELATED WORK

In this section, we provide a concise review of the main methods in the field of IRST, with a particular emphasis on research related to MIRST detection. Existing MIRST detection methods can be broadly categorized into model-driven methods and data-driven methods. The former primarily relies on filtering or handcrafted optimization models for feature extraction, while the latter utilizes deep learning methods to automatically learn feature representations from large-scale data.

### A. Model-driven schemes for IRST

Model-driven infrared small target detection methods can be divided into two categories: filtering methods based on local priors and optimization methods based on non-local priors.

Filtering methods operate under the background consistency assumption, estimating the image background and enhancing

targets via background subtraction. Classical methods like Top-Hat [6] and two-dimensional least mean square(TDLMs) [7] perform well in uniform backgrounds but struggle in complex cluttered environments. Subsequent improvements include Human Visual System (HVS)-based methods that leverage target saliency characteristics [20], [21], [22].

In contrast, optimization methods exploit the non-local correlation of backgrounds and target sparsity, achieving target-background separation through model formulation. Early methods assumed low-rank background subspaces, with the infrared patch-image (IPT) model [8] framing detection as a low-rank and sparse decomposition problem. This inspired numerous subspace-based variants [23], [24], [25]. Further developments include designing the reweighted infrared patch tensor [9], formulating the non-convex rank approximation Minimization[10], proposing the partial sum of tensor nuclear norm[26], and incorporating local contrast energy or hyper total variation to improve robustness [27], [28].

To incorporate temporal information, sequence-based tensor methods have been developed, extending prior spatial models into the spatio-temporal domain. Representative approaches include extending multi-subspace learning to the tensor domain [11], constructing spatio-temporal tensors with overlapping patches [29], and extracting non-overlapping patches across frames via sliding windows [12]. Further improvements involve designing specialized regularization methods combined with non-convex tensor rank approximation [30], imposing constraints on Tucker decomposition factor matrices [13], and incorporating total variation on sparse representation matrices [31]. Advanced methods also leverage sparse regularization to enhance target-background distinction [32] or extend tensor decomposition to four-dimensional representations [33].

### B. Data-driven schemes for IRST

Model-driven methods often rely on manual parameter tuning and idealized mathematical models, whereas data-driven methods employ deep learning to automatically learn features from large-scale data, enabling end-to-end infrared small target detection. Deep learning-based approaches are broadly divided into single-frame and multi-frame methods. Single-frame detection focuses on spatial feature extraction, primarily through enhanced network architectures such as multi-scale fusion modules[34], [35], optimized U-shaped structures[36], and the incorporation of mathematical priors [37], [38]. Multi-frame detection further incorporates temporal information. Mainstream supervised models can be classified into two paradigms: the iterative feature propagation mode and the sliding-window mode.

The iterative feature propagation mode processes image sequences frame-by-frame. The output for each frame includes both the detection result and features that aid in the processing of the next frame. In this mode, Ma et al. [14] proposed a temporal-spatial information fusion network (TSIF) to adaptively fuse inter-frame features. Zhuang et al. [15] introduced a temporal-semantic interaction network (TSI-Net) to capture subtle motion changes between frames. Chen et al. [39] designed a linking-aware sliced network (LASNet),

which addresses confusion caused by dense motion through a motion mask loss function. Liu et al. [40] incorporated Bi-Conv-LSTM and 3D convolution structures to learn the motion patterns of infrared targets. Lin et al. [41] proposed a general and effective time shift module (TSM), which shifts a portion of channels along the temporal dimension to facilitate inter-frame information exchange. Some studies embed single-frame detection modules into the iterative feature propagation mode to enhance spatial feature extraction. Li et al. [42] extracted spatial saliency features via a detection head, then input the features of five consecutive frames into a direction-coded temporal U-shape module (DTUM) for motion modeling. Ying et al. [16] proposed a recurrent feature refinement framework (RFR) which introduces deformable convolution and a pyramid structure to improve the accuracy of the inter-frame registration and strengthens the extraction of position information via a detection head, making it particularly suitable for long sequence detection. The advantages of the iterative feature propagation mode include computational efficiency for only requiring single-frame computation at the same time and support for long-sequence reasoning. Its drawbacks are the inconsistency between training and inference mechanisms, time-varying error accumulation, and inferior detection performance in the initial frames due to insufficient temporal information.

In contrast, the sliding-window mode inputs a fixed-length window of multiple frames into the network and outputs the detection results for all frames within that window. Each time, a sequence of frames are fed directly into the network, producing the corresponding outputs. In this paradigm, Luo et al. [17] proposed deformable feature alignment and refinement (DFAR), which performs feature registration and fusion within a sliding five-frame window. Shen et al. [18] first established spatio-temporal context associations in shallow layers before feeding them into a U-shaped transformer structure. Huang et al. [43] and Li et al. [44] incorporated the idea of trajectory energy accumulation into the MIRSDT model, converting temporal characteristics into spatial saliency. Cui et al. [19] proposed a multiscale spatio-temporal feature combined network (MSTCNet), which integrates CNN and RNN modules and introduces scale-position invariant feature learning to enhance generalization capability. Studies [45], [46], [47] have achieved multi-frame detection by extracting spatial and temporal features in parallel and then fusing them. The sliding-window mode effectively integrates spatio-temporal features. However, its limitations lie in the fact that the window length restricts the model's receptive field, and the computational load increases significantly with the window size. This also somewhat limits the number of frames that can be input to the model at once.

### III. METHODOLOGY

#### A. Overall Framework

As illustrated in Fig. 1, we present a sparse frames-based spatio-temporal feedback semantic network (FeedbackSTS-Det), which fundamentally rethinks temporal modeling in infrared small target detection. Built upon a balanced 3D Res-UNet backbone [48], [49], our network processes sliding

windows by partitioning the continuous temporal image data into shorter sequences (denoted as *Seq*) of length  $D$ , with each *Seq* sequentially extracted as input. This approach maintains consistency between the training and inference processes, ensuring the stability of model performance during actual deployment.

The encoder phase incorporates five consecutive forward spatio-temporal semantic refinement modules (FSTSRM), while the decoder phase employs four successive backward spatio-temporal semantic refinement modules (BSTSRM). Both modules critically integrate our novel sparse semantic module (SSM), which operates by strategically grouping frames at intervals, propagating semantics within each group using the Basic Feedback Module (BFM), and then reassembling the sequence. Together, the FSTSRM and BSTSRM construct a closed-loop semantic association mechanism.

This overall framework will be detailed in Section III-B, whereas the SSM will be elaborated in Section III-C. To alleviate the excessive growth of floating-point operations during iterative feature propagation, we deliberately set the base channel number of the overall framework to 8, ensuring that the deepest layer maintains a maximum channel count of 128.

#### B. Spatio-Temporal Semantic Feedback Strategy

The spatio-temporal semantic feedback strategy establishes a closed-loop semantic association mechanism, which comprises the FSTSRM and BSTSRM modules described in detail below.

1) *Forward Spatio-Temporal Semantic Refinement Module*: The forward spatio-temporal semantic refinement module (FSTSRM) establishes the forward propagation path in our spatio-temporal feedback system, progressively building spatio-temporal semantic understanding across frames. Given input features  $\mathbf{X} \in \mathbb{R}^{C \times D \times H \times W}$ , it operates through two distinct pathways. The context preservation branch maintains spatial integrity and local spatio-temporal semantics by using two consecutive 3D convolutions with a kernel size of 3, each followed by 3D Batch Normalization. The spatio-temporal semantic propagation branch enables forward spatio-temporal semantic flow through sparse temporal processing, sequentially processing features through a 3D convolution with a kernel size of 1 and then an SSM module. The formal descriptions of these two branches are given by Eq. (1) and Eq. (2), respectively.

$$\mathbf{X}_{\text{context}} = (\text{BN} \circ C_{3 \times 3 \times 3})^{(2)}(\mathbf{X}) \quad (1)$$

$$\mathbf{X}_{\text{prop}} = \text{SSM}(C_{1 \times 1 \times 1}(\mathbf{X})) \quad (2)$$

where  $C_{3 \times 3 \times 3}$  and  $C_{1 \times 1 \times 1}$  denote 3D convolutions with kernel sizes of 3 and 1, respectively,  $\text{BN}(\cdot)$  is the batch norm operation, and the operator  $\mathcal{T}_{\text{SSM}}(\cdot)$  represents the processing through the SSM, whose details are provided in Fig. 1 (d) and Section III-C. The enriched forward spatio-temporal semantics are then generated by the element-wise addition of the outputs from these two modules.:

$$\mathbf{Y}_{\text{FSTSRM}} = \mathbf{X}_{\text{context}} \oplus \mathbf{X}_{\text{prop}} \quad (3)$$

where  $\oplus$  represents element-wise addition.

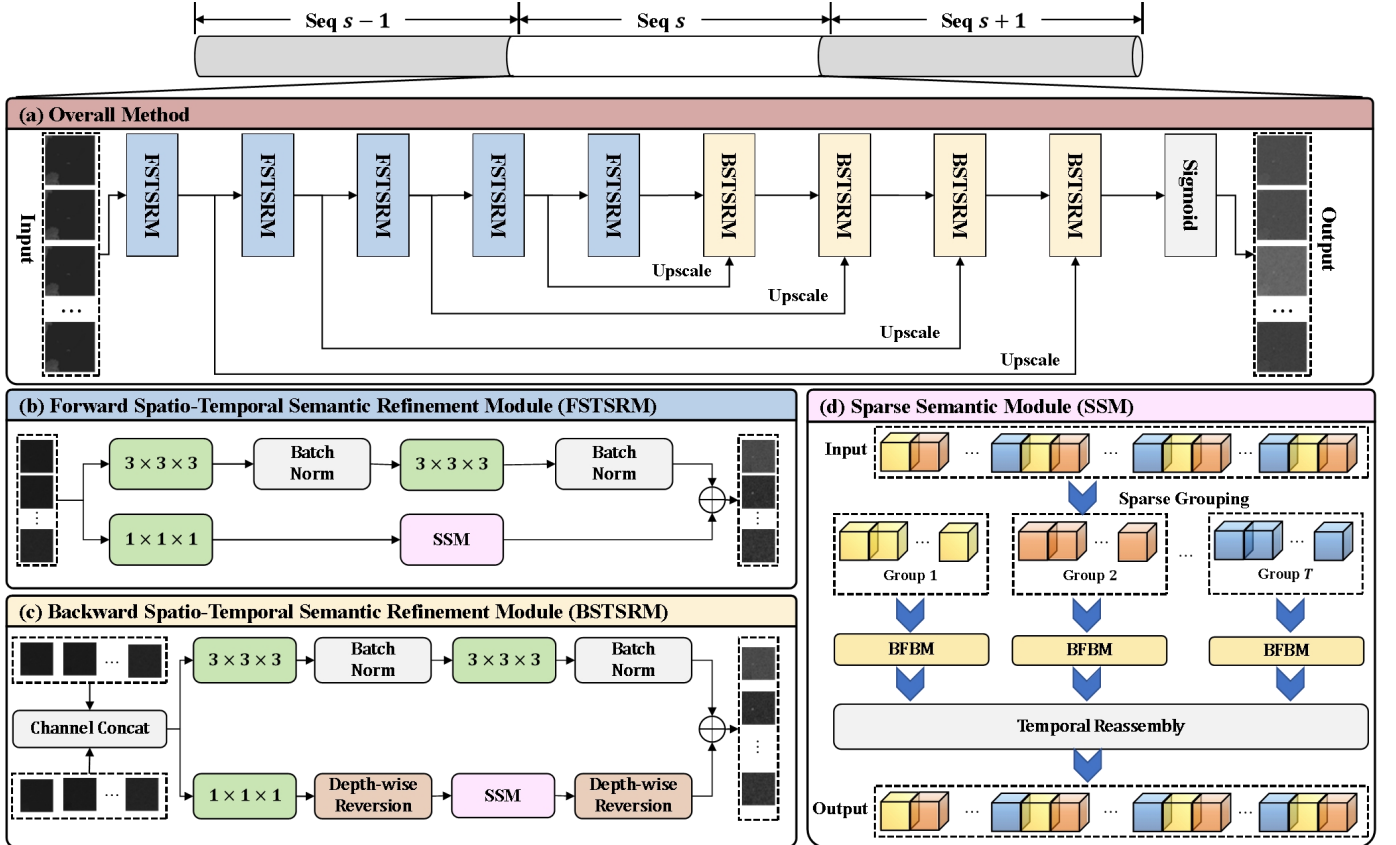


Fig. 1. Overall procedure of FeedbackSTS-Det model for ISTD. (a) presents the overall framework. (b) denotes forward spatio-temporal semantic refinement module (FSTSRM), (c) illustrates backward spatio-temporal semantic refinement module (BSTSRM), and (d) describes sparse semantic module (SSM).

2) *Backward Spatio-Temporal Semantic Refinement Module*: The backward spatio-temporal semantic refinement module (BSTSRM) implements the feedback component by reversing temporal dependencies, allowing later spatio-temporal semantic understanding to refine earlier interpretations through retrospective analysis. While its basic structure remains consistent with the FSTSRM, it receives outputs from the adjacent deeper decoder module and the peer-level FSTSRM module, then concatenates them along the channel dimension. For the BSTSRM at the  $f$ -th layer, its input formulation is given below:

$$\mathbf{X}_{\text{in}} = \text{Concat}(\mathbf{Y}_{\text{dec}}^{(f+1)}, \mathbf{Y}_{\text{FSTSRM}}^{(f)}; \text{dim} = 1) \quad (4)$$

where the superscript  $(f)$  denotes the  $f$ -th layer module. BSTSRM reuses the same context preservation branch as defined in Eq. (1) and employs a reversed spatio-temporal semantic propagation path for retrospective refinement:

$$\mathbf{X}_{\text{refine}} = \text{DR}(\text{SSM}(\text{DR}(C_{1 \times 1 \times 1}(\mathbf{X})))) \quad (5)$$

where the depth-wise reversal operator  $\text{DR}(\cdot)$  enables retrospective spatio-temporal semantic analysis by swapping the order of frames along the temporal dimension  $D$ :

$$\text{DR}(\mathbf{X})_{c,d,h,w} = \mathbf{X}_{c,D-d+1,h,w} \quad (6)$$

The complete BSTSRM output integrates both the preserved context and the refined spatio-temporal semantics, following the same fusion principle as the FSTSRM:

$$\mathbf{Y}_{\text{BSTSRM}} = \mathbf{X}_{\text{context}} \oplus \mathbf{X}_{\text{refine}} \quad (7)$$

This feedback strategy creates a system where FSTSRM establishes initial interpretations while BSTSRM provides corrective feedback, continuously refining target spatio-temporal semantics and suppressing background clutter through iterative improvement.

### C. Sparse Semantic Module

The sparse semantic module (SSM) is a core component that implements our proposed sparse semantic method, as illustrated in Fig. 1 (d). It is designed to achieve efficient long-range temporal modeling by strategically processing a subset of frames, thereby reducing computational overhead while enhancing feature propagation across distant frames. The SSM operates in three consecutive stages: sparse grouping, intra-group spatio-temporal semantic propagation, and temporal reassembly.

1) *Sparse Grouping*: Given an input feature sequence of length  $D$ , denoted as  $\{I_1, I_2, \dots, I_D\}$ , the SSM first partitions it into several disjoint groups via interval sampling with a fixed step size  $T$ . Formally, the  $x$ -th group  $\mathcal{G}_x$  ( $x \in [1, T] \cap \mathbb{N}$ ) is defined as:

$$\mathcal{G}_x = \{I_x, I_{x+T}, \dots, I_{x+M_x T}\} \quad (8)$$

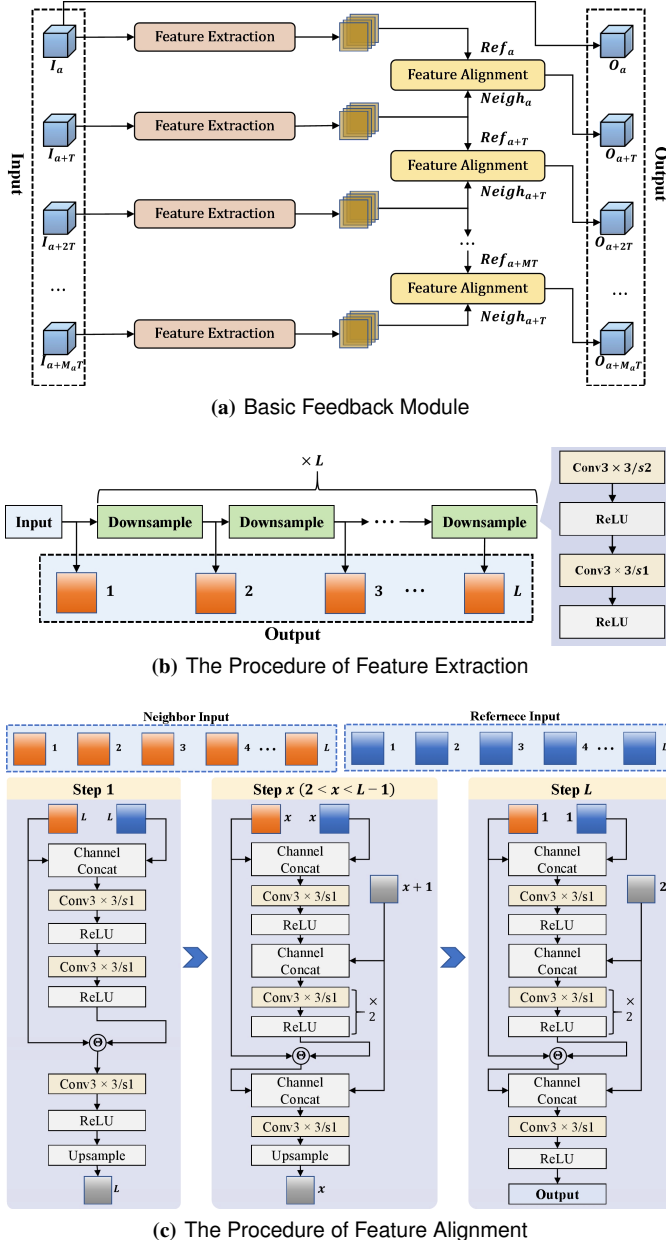


Fig. 2. Basic feedback module (BFBM). (a) presents the framework of the BFBM module, which is embedded within the SSM. (b) details the procedure of feature extraction in BFBM, and (c) shows the procedure of feature alignment module in BFBM.

where  $M_x = \lfloor \frac{D-x}{T} \rfloor$  represents the number of subsequent frames sampled in this group. This grouping strategy establishes  $T$  parallel processing streams, each focusing on frames separated by a frame interval of  $T$ . It offers three primary benefits: computational efficiency by reducing direct frame-to-frame interactions, enhanced robustness to transient noise as the larger interval helps filter out short-lived clutter, and emphasis on genuine target motion patterns that persist over longer time spans.

2) *Intra-Group Spatio-Temporal Semantic Propagation*: As shown in Fig. 1 (d), assuming a sparse interval of  $T$ , the spatio-temporal semantic information within each group  $\mathcal{G}_a$  (where  $a \in [1, T] \cap \mathbb{N}$ ) is processed by the same module,

called the basic feedback module (BFBM). The workflow of BFBM is shown in Fig. 2 (a). For each group, all frames except the first one undergo two procedures which are feature extraction and feature alignment. Both procedures are adapted from the pyramid deformable alignment (PDA) module [16] and are deliberately decoupled in our design to reduce redundant computation. Although the first frame is not processed in BFBM apparently, the overall design is compensated by the spatio-temporal semantic feedback strategy described in Section III-C.

For a PDA [16] with  $L$  layers, as illustrated in Fig. 2 (b), the procedure of feature extraction downsamples the input  $L$  times to obtain multi-scale features. From shallow to deep layers,  $L$  corresponding feature maps of different scales are obtained. Then, the procedure of feature alignment presented in Fig. 2 (c) aligns adjacent feature maps, using one as the reference input and the other as the neighbor input. Both inputs are processed through  $L$  steps. Following a recursive pyramid scheme, the alignment proceeds from the  $L$ -th layer to the first layer in a bottom-up manner. At each level, deformable convolutions [50], [51] combined with upsampling are applied to register features across different scales. After the final ( $L$ -th) step, the aligned feature output is obtained.

Overall, for an input group  $\mathcal{G}_a = \{I_a, I_{a+T}, \dots, I_{a+M_a T}\}$ , let  $x \in [1, M_a] \cap \mathbb{N}$ , the output for each frame is computed as follows:

$$O_a = I_a \quad (9)$$

$$O_{a+xT} = \text{FA}(\text{FE}(I_{a+xT}), \text{FE}(I_{a+(x-1)T})) \quad (10)$$

where  $\text{FE}(\cdot)$  and  $\text{FA}(\cdot)$  represent the procedure of feature extraction and the procedure of feature alignment, respectively. After processing all  $M_a + 1$  frames in  $\mathcal{G}_a$ , the group yields a set of refined output features:

$$\mathcal{O}_a = \{O_a, O_{a+T}, \dots, O_{a+M_a T}\} \quad (11)$$

3) *Temporal Reassembling*: In the final stage, the outputs from all  $T$  groups are interleaved and sorted according to their original temporal indices to reconstruct a complete, coherent feature sequence of length  $D$ :

$$\mathbf{Y}_{\text{SSM}} = \text{Merge}(\mathcal{O}_1, \mathcal{O}_2, \dots, \mathcal{O}_T) \quad (12)$$

where  $\text{Merge}(\cdot)$  is a simple concatenation and sorting operation that reconstructs the full feature sequence  $\{O_1, O_2, \dots, O_D\}$ , preserving the temporal order. This reassembling distributes the semantically enhanced features from the sparse frames back to all positions in the sequence, providing refined inputs for subsequent network layers.

4) *Parameter Configuration*: Empirically, we set the number of layers  $L$  in both the feature extraction and feature alignment procedures of the BFBM to 2, which achieves a good balance between alignment accuracy and computational cost. The sampling step  $T$  is a key hyperparameter; our experiments demonstrate that values of 2, 3, or 4 yield optimal performance, effectively trading off between temporal coverage and processing efficiency.

## IV. EXPERIMENT

In this section, we first describe the experimental setup, including evaluation metrics and implementation details. Then, we evaluate our method against other baseline and state-of-the-art approaches on both SIRST and MIRST tasks. Finally, we present ablation studies to validate the effectiveness of our design.

### A. Datasets and Implementation

1) *Datasets*: NUDT-MIRSDT [42] and IRSatVideo-LEO [16] datasets are employed to evaluate the performance of the proposed FeedbackSTS-Det. Specifically, the NUDT-MIRSDT [42] dataset contains 120 sequences and 12,000 images. Image dimensions vary across sequences, with widths ranging from 101 to 442 pixels and heights from 96 to 327 pixels. The dataset includes diverse infrared scenes, such as clouds, oceans, and land surfaces. Each sequence is generated by applying local perturbations and synthetic noise to infrared imagery. Meanwhile, IRSatVideo-LEO [16] comprises 200 sequences with a total of 91,022 images. This semi-synthetic dataset is constructed by combining real satellite imagery with simulated satellite motion trajectories. Both datasets are equipped with high-quality pixel-level mask annotations, making them suitable benchmarks for evaluating the temporal segmentation performance of detection models.

2) *Metrics*: In this paper, we adopt a mainstream evaluation framework [35], [52] for infrared small target detection models, incorporating pixel-level metrics (Intersection over Union (IoU), F-measure, False Alarm Rate (Fa)) and object-level metrics (Detection Rate (Pd), along with the Receiver Operating Characteristic (ROC)). In experiments, the threshold for object-level evaluation is typically set at 0.5.

3) *Implementation Details*: We use Soft-IoU loss [51] and the Adam optimizer with a MultiStepLR scheduler, starting at  $1e^{-5}$  and halving at epochs [5, 10, 15, 20, 25, 30]. Training lasts 30 epochs from scratch, implemented in PyTorch on six NVIDIA RTX 4090 GPUs.

Training strategies varies by dataset. For IRSatVideo-LEO [16], we randomly crop  $1024 \times 1024$  images to  $256 \times 256$  to preserve small targets, following RFR's approach<sup>1</sup>. For NUDT-MIRSDT [42], we avoid cropping to retain full-image context. Both datasets then undergo the same augmentations (horizontal/vertical/channel flips, transpositions) before resizing to  $256 \times 256$ .

To ensure a consistent evaluation protocol, We exclude the “Mix” folder from NUDT-MIRSDT, which contains simulated sequences, to focus evaluation on authentic infrared sequences from its “images” and “masks” folders.

### B. SOTA Comparisons

We compare the proposed FeedbackSTS-Det against state-of-the-art methods in both single-frame and multi-frame infrared small target detection. For single-frame infrared small target detection, evaluated methods include three model-driven approaches: TopHat [6], NRAM [10], and PSTNN [26]; and

seven data-driven methods: ACM [34], ALCNet [53], DNANet [52], RDIAN [38], ISTDU-Net [54], RPCANet [55], and L2SKNet\_FPN [56]. For multi-frame infrared small target detection, comparisons include seven model-driven methods (MSLSTIPT [11], NFTDGSTV [13], RCTV [31], IMNN-LWEC [57], SRSTT [32], ASTTV-NTLA [30], 4DISDT [33]) and five data-driven methods (DNANet\_DTUM [42], ALCNet\_DTUM [42], ResUNet\_DTUM [42], ACM\_RFR [16], ResUNet\_RFR [16]). For data-driven MIRST methods, all metrics except FLOPs follow original sequence lengths: RFR-based methods [16] take 20 frames as input, while DTUM-based methods [42] take 5. In the comparative experiments of this study, our model—which is capable of processing an arbitrary number of input frames—was set to take 11 frames as input. Its variants using different sampling intervals  $t$  are denoted as FeedbackSTS-Det-T $t$ . When  $t = 1$ , the model bypasses interval sampling in TSIFPM. All models are retrained from scratch on both IRSatVideo-LEO [16] and NUDT-MIRSDT [42] datasets under identical settings for fair comparison.

1) *Quantitative Results*: Table I presents a comprehensive comparison of state-of-the-art methods on the IRSatVideo-LEO [16] and NUDT-MIRSDT [42] using multiple evaluation metrics. Our proposed FeedbackSTS-Det variants consistently demonstrate superior performance across both datasets, with each sampling interval configuration exhibiting distinct advantages. The FeedbackSTS-Det-T2 variant achieves the most balanced and outstanding performance overall. On the NUDT-MIRSDT [42] dataset, it obtains the best results in four key metrics:  $mIoU$ ,  $F_1$ ,  $P_d$ , and  $AUC$ , while maintaining the second-lowest false alarm rate. Similarly, on the IRSatVideo-LEO [16] dataset, it delivers competitive detection accuracy with an exceptionally low false alarm rate of  $5.5 \times 10^{-7}$ , indicating its strong robustness in practical scenarios. The FeedbackSTS-Det-T3 and FeedbackSTS-Det-T4 variants also show remarkable capabilities, particularly in specific metrics. FeedbackSTS-Det-T3 achieves the second-best performance in  $P_d$  and  $AUC$  on NUDT-MIRSDT [42], while FeedbackSTS-Det-T4 excels on IRSatVideo-LEO [16] with the highest  $P_d$  of 0.9648 and  $AUC$  of 0.9816. This performance progression across sampling intervals reveals an important trade-off: larger intervals reduce computational complexity while maintaining competitive detection accuracy.

Notably, all three FeedbackSTS-Det variants significantly outperform both traditional model-driven methods and contemporary data-driven approaches. While methods like DNANet\_DTUM [42] and ResUNet\_RFR [16] show respectable results, they are consistently surpassed by our proposed framework across virtually all metrics. This performance advantage is achieved while maintaining reasonable computational requirements, with all FeedbackSTS-Det variants utilizing only 5.68M parameters and FLOPs decreasing from 79.39G to 68.50G as the sampling interval increases. The consistent superiority of FeedbackSTS-Det across different sampling configurations validates the effectiveness of our architectural design and demonstrates its robustness for infrared small target detection in diverse operational scenarios.

The ROC results are presented in Fig. 3. As shown in

<sup>1</sup><https://github.com/XinyiYing/RFR/>.

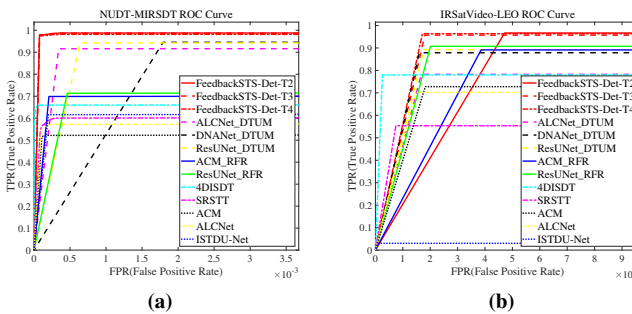


Fig. 3. ROC curves on two benchmark datasets. (a) ROC Curve on NUDT-MIRSDT. (b) ROC Curve on IRSatVideo-LEO.

Fig. 3(a), all FeedbackSTS-Det variants achieve a faster increase in TPR, reaching 1 more quickly than other models. In the more challenging IRSatVideo-LEO dataset (Fig. 3(b)), although FeedbackSTS-Det-T2 exhibits a slower initial TPR rise, it ultimately reaches the maximum value faster. Meanwhile, FeedbackSTS-Det-T3 and FeedbackSTS-Det-T4 maintain strong TPR growth throughout the entire phase, confirming their robust detection performance.

2) *Qualitative Results*: Qualitative results are presented in Fig. 4. The selected examples are organized as follows: Rows 1–2 illustrate easy scenes from IRSatVideo-LEO [16]; Rows 3–4 depict medium scenes; Rows 5–6 present challenging scenes from the same dataset; and Rows 7–8 show sequence samples from NUDT-MIRSDT [42]. The scenes encompass satellite, aerial, and maritime imagery captured from a vertical perspective. It can be observed that traditional model-driven methods, including low-rank and sparse representation techniques such as PSTNN [26] and SRSTT [32], exhibit limited detection performance in these scenes. The typical single-frame low-rank and sparse infrared small target detection method, PSTNN [26], produces significant false alarms in most satellite nadir-view scenes except for the sequence "EastNorthAsia25\_43", and fails to detect targets correctly in "Sequence92" and "Sequence96". SRSTT [32], as a representative multi-frame low-rank and sparse detection method, generates substantial false alarms across all sequences and exhibits missed detections in several satellite view sequences. Data-driven multi-frame methods show noticeable improvement, yet still exhibit certain limitations. Except for "Sequence96", ALCNet\_DTUM [42] produces false alarms in all other sequences, with particularly severe cases in "Sequence92". RFR-based [16] frameworks (e.g., ResUNet\_RFR [16] and ACM\_RFR [16]) yield significant false alarms in sequences such as "EastNorthAsia0\_97", "EastAustralia3\_94", "EastAustralia5\_07", and "EastNorthAsia25\_43". However, ACM\_RFR [16] achieves relatively good detection performance on "Sequence96". In contrast, it can be observed that all of the variants of our FeedbackSTS-Det achieve the optimal performance across all scenarios and all difficulty levels of datasets, specifically in terms of accurate target localization, low false alarm rate, and the morphological accuracy of detected targets.

### C. Ablation Study

This subsection presents experiments on FeedbackSTS-Det and its variants, aiming to verify the potential advantages of our proposed modules and key design decisions. If not stated explicitly, we set the temporal sampling interval to 2.

1) *Spatio-Temporal Semantic Feedback Strategy*: Introduced in Section III-B, the spatio-temporal semantic feedback strategy is designed to strengthen inter-frame feature linkages for better infrared small target detection. Our approach is built upon a 3D U-Net backbone [49]. This framework comprises five downsampling layers: conv\_1, conv\_2, conv\_3, conv\_4, and conv\_5; and four upsampling layers: dec\_conv\_1, dec\_conv\_2, dec\_conv\_3, and dec\_conv\_4. A systematic comparison of the ablated variants of this feedback design is provided in Table II.

This ablation study is designed to validate the effectiveness of our proposed framework by contrasting it against several alternative configurations, including unidirectional (All-Fwd, All-Bwd), partial semantic feedback (Part-FB1, Part-FB2), and feedback-disabled schemes (Dec-NoFB, Enc-NoFB).

As summarized in Table II, while simpler configurations like Enc-NoFB achieve the lowest parameter count and FLOPs, our optimal method, Full-FB, strikes a critical balance. It maintains full feature interaction capabilities in both the encoder and decoder, incurring only a modest increase in computational cost compared to the most constrained variants. Subsequent experiments confirm that the proposed spatio-temporal semantic feedback framework is a necessary and efficient component for accurate target localization, shape delineation, and false alarm suppression.

For consistent performance evaluation where higher values indicate better results across all metrics, including  $mIoU$ ,  $F_1$ ,  $P_d$ , and  $AUC$ , we introduce the false alarm suppression rate (FSR), defined as follows:

$$FSR = 1 - F_a \times 10^3 \quad (13)$$

As illustrated in Fig. 5, we benchmark all spatio-temporal semantic feedback variants from Table II against our optimal method, Full-FB, on the NUDT-MIRSDT [42] dataset. The evaluation uses five metrics ( $mIoU$ ,  $F_1$ ,  $P_d$ ,  $FSR$ ,  $AUC$ ) under a fixed input size of  $5 \times 256 \times 256$ , and results show the clear superiority of our method across all metrics.

The visual comparisons corresponding to the methods in Table II are provided in Fig. 6, Fig. 7, Fig. 8, Fig. 9, and Fig. 10. For clarity, targets are annotated with bounding boxes positioned at image corners, with distinct colors assigned to different targets for easy cross-reference. The effectiveness of backward feedback in the decoder is demonstrated by comparing Full-FB with alternative designs. First, in Fig. 6, Full-FB shows progressively stronger suppression and clearer targets during backward feedback (frames #0504 to #0500), while Dec-NoFB performs poorly. Second, Fig. 8 reveals that the All-Fwd method yields unclear targets in initial frames (#0500, #0501) during forward feedback, whereas Full-FB exhibits this limitation only in the initial frame (#0504) of its backward process. Moreover, in Fig. 7 and Fig. 9, targets in the second row (Full-FB) are consistently clearer than those

TABLE I

THE RESULTS OF  $mIoU$  ( $\times 10^{-2}$ ),  $F_1$  ( $\times 10^{-2}$ ),  $P_d$  ( $\times 10^{-2}$ ),  $F_a$  ( $\times 10^{-6}$ ) AND  $AUC$  ( $\times 10^{-2}$ ) ARE ACHIEVED BY DIFFERENT METHODS ON THE DATASETS IRSATVIDEO-LEO[16] AND NUDT-MIRSDT [42]. "PARAMS." REPRESENTS THE NUMBER OF PARAMETERS. FLOPS ARE CALCULATED BASED ON AN INPUT SEQUENCE SCALE OF  $11 \times 256 \times 256$ . THE BEST-PERFORMING RESULTS ARE INDICATED IN RED FONT, WHILE THE SECOND-BEST RESULTS ARE SHOWN IN BLUE FONT.

Method	Params(M)	FLOPs(G)	NUDT-MIRSDT					IRSatVideo-LEO				
			$mIoU \uparrow$	$F_1 \uparrow$	$P_d \uparrow$	$F_a \downarrow$	$AUC \uparrow$	$mIoU \uparrow$	$F_1 \uparrow$	$P_d \uparrow$	$F_a \downarrow$	$AUC \uparrow$
TopHat [6]	-	-	4.32	8.29	15.42	70.20	68.66	4.18	8.03	27.46	3.26	63.73
NRAM [10]	-	-	2.98	5.78	8.68	26.80	59.89	1.51	2.97	9.45	0.20	54.68
PSTNN [26]	-	-	13.03	23.06	21.62	84.92	64.64	3.50	6.76	46.29	61.31	73.14
ACM [34]	0.398	4.426	36.94	53.95	51.00	39.91	76.08	30.53	46.78	72.87	7.33	86.38
ALCNet [53]	0.427	4.157	32.26	48.79	54.65	65.38	78.58	31.36	47.75	70.27	5.21	85.12
DNA-Net [52]	4.697	71.306	27.51	43.15	60.00	211.94	80.04	0.13	0.27	0.92	0.21	50.44
RDIAN [38]	0.217	40.902	19.33	32.40	61.06	509.90	80.74	0.10	0.19	6.73	2009.97	53.67
ISTDU-Net [54]	2.752	87.388	33.45	50.13	60.88	111.24	80.78	0.47	0.93	3.09	0.96	51.51
RPCANet [55]	0.680	490.255	0.02	0.05	10.47	495831.30	73.74	0.00	0.00	0.65	499730.39	63.20
L2SKNet_FPN [56]	1.071	66.085	21.12	34.88	43.06	92.03	71.85	1.09	2.15	47.67	362.75	73.23
MSLSTIPT [11]	-	-	13.76	24.19	21.66	125.26	76.25	4.68	8.94	36.71	12.41	68.35
NFTDGSTV [13]	-	-	2.41	4.71	5.50	307.22	64.46	0.99	1.97	50.16	191.84	75.06
RCTV [31]	-	-	0.34	0.68	0.18	1.40	52.55	8.74	16.07	39.31	0.93	69.65
IMNN-LWEC [57]	-	-	6.04	11.40	13.51	209.38	64.57	1.51	2.97	46.00	265.21	72.97
SRSTT [32]	-	-	12.18	21.72	21.16	444.36	80.01	12.68	22.51	55.40	6.63	77.68
ASTTV-NTLA [30]	-	-	0.78	1.55	0.36	52.54	53.84	0.80	1.59	50.88	206.00	75.42
4DISDT [33]	-	-	10.66	19.26	15.92	105.03	82.97	23.13	37.58	78.16	1.81	89.00
DNANet_DTUM [42]	1.205	97.757	10.44	18.91	94.29	1726.77	97.18	38.88	55.99	88.24	6.31	93.93
ALCNet_DTUM [42]	0.842	16.897	35.67	52.58	91.82	175.71	95.78	35.49	52.39	79.18	2.53	89.13
ResUNet_DTUM [42]	0.298	22.772	24.33	39.13	95.65	499.13	97.09	38.22	55.30	89.52	6.58	94.61
ACM_RFR [16]	0.504	40.842	29.98	46.13	69.24	135.79	84.92	24.68	39.59	89.18	16.88	94.56
ResUNet_RFR [16]	1.012	79.801	30.98	47.31	70.94	286.67	85.64	37.49	54.54	90.82	6.02	95.36
FeedbackSTS-Det-T2 (Ours)	5.678	79.386	52.24	68.63	97.41	14.42	99.38	43.50	60.63	95.28	0.55	97.46
FeedbackSTS-Det-T3 (Ours)	5.678	73.941	51.55	68.03	97.29	19.23	99.32	41.96	59.11	95.83	4.51	97.84
FeedbackSTS-Det-T4 (Ours)	5.678	68.496	51.95	68.38	96.65	18.45	99.05	43.42	60.54	96.48	3.07	98.16

in the first row (the compared methods), highlighting the benefit of forward feedback in the encoder. Finally, Fig. 10 indicates that removing spatio-temporal semantic feedback modules in certain layers degrades target feature extraction, further underscoring the necessity of the complete feedback framework.

2) *Sparse Semantic Module*: The sparse semantic module (SSM), a core innovation introduced in Section III-C, aims to enhance inter-frame feature propagation by strategically skipping frames. To comprehensively evaluate its efficacy, we design three sets of ablation studies to validate its dual benefits: significantly improving computational efficiency and strengthening the model's capability for effective feature propagation in long temporal sequences.

For clarity, we use T1 to denote the baseline without temporal sampling, and T2, T3, T4 as shorthands for FeedbackSTS-Det-T2, -T3, and -T4, with sparse frame sampling intervals of 2, 3, and 4, respectively. The computational efficiency of the model under different settings is summarized in Table III, which reports FLOPs and FPS for various sequence lengths  $L$  and temporal sampling intervals  $T$  based on an input image scale of  $256 \times 256$ . The results demonstrate that for a fixed  $T$ , longer sequences  $L$  lead to higher FLOPs and generally lower FPS. Conversely, increasing the temporal

sampling interval  $T$  consistently reduces computational cost and improves inference speed across all sequence lengths. For instance, when the sequence length is set to  $L = 9$ , the computational cost measured in FLOPs decreases from 68.42G for  $T = 1$  to 52.08G for  $T = 4$ , while the inference speed (FPS) increases from 7.5 to 13.7, representing a substantial improvement of 82.6% in processing efficiency. This analysis confirms that larger temporal sampling intervals enhance computational efficiency, especially for long sequences.

To evaluate the efficacy of the temporal sampling mechanism, we conduct a comparative analysis between the T2 condition (with a temporal sampling interval of length 2) and the T1 condition (without temporal sampling) on the IRSatVideo-LEO [16], using  $P_d$  and  $F_a$  as key metrics. As shown in Fig. 11 (a), the  $P_d$  for T2 increases monotonically with the sequence length  $L$ , whereas the  $P_d$  for T1 exhibits significant and unstable fluctuations. From Fig. 11 (b), it is observed that the  $F_a$  for T2 remains consistently stable within a narrow range as  $L$  increases. In contrast, the  $F_a$  for T1 varies drastically and is markedly higher than that of T2. In summary, the sparse frame sampling module significantly enhances target detection capability while effectively suppressing false alarms over long sequences, demonstrating its robust ability to propagate inter-frame features compared to the baseline T1

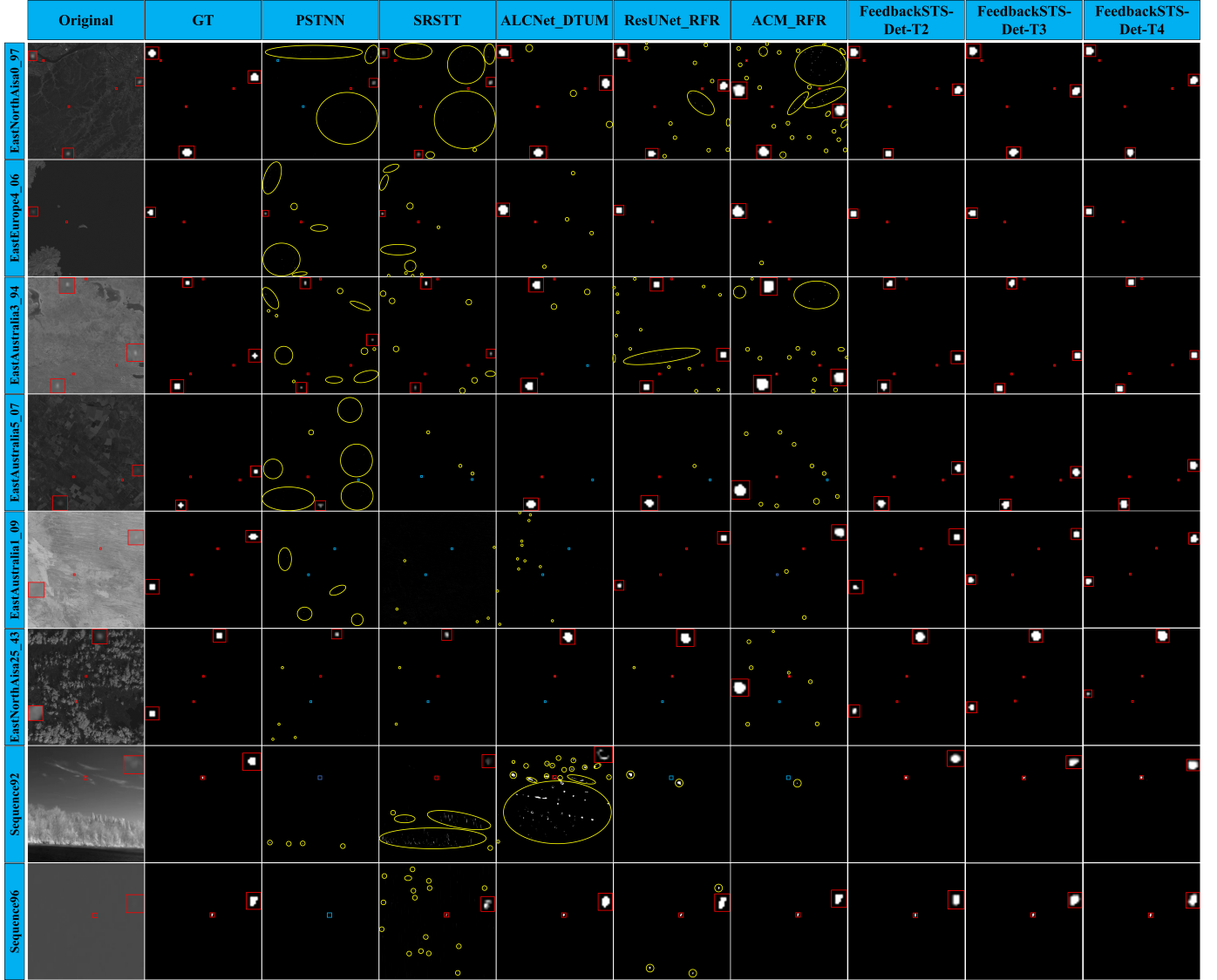


Fig. 4. Qualitative results of different methods. For better visual presentation, the target regions are highlighted with red boxes and then displayed as zoomed-in views. Missed detections and false alarms are marked with blue and yellow circles, respectively.

condition.

To investigate the capability of different sparse frame sampling intervals in extracting targets under varying input window sizes, we evaluate the effect of the input sequence length  $L$  on the detection probability  $P_d$  cross different sampling intervals using the IRSatVideo-LEO [16], as shown in Fig. 12. It could be observed that  $P_d$  increases with  $L$  for all sampling intervals, validating that the sparse frame sampling module successfully enhances inter-frame dependencies in long sequences. Moreover, a longer sampling interval is generally associated with improved performance at an equivalent sequence length. An exception is noted at  $L = 11$ , where T4 underperforms T3; however, T4 demonstrates superior performance at  $L = 13$ .

Our proposed FeedbackSTS-Det architecture can be decomposed into a top-down encoder, comprising the sequential layers: FSTS1, FSTS2, FSTS3, FSTS4, FSTS5, and a bottom-up decoder, consisting of BSTSRM1,

BSTSRM2, BSTSRM3, BSTSRM4. The visual results of selected sub-modules under varying sequence lengths ( $L$ ) and temporal sampling intervals ( $T$ ) are presented in Figs. 13 to Fig. 15. For clarity, the targets in these figures are annotated with bounding boxes placed in the corners of the image, with each color corresponding to a distinct target. The results demonstrate that in both the encoding and decoding stages, an increase in the sparse frame sampling interval  $T$  generally leads to sharper target features against the background and more effective suppression of false alarms.

3) *3D Modified Frameworks*: To evaluate the effectiveness of 3D modified, we compare several single-frame infrared detection models, including ACM [34], DNA-Net [52], and UIUNet [36], with their 3D-modified versions on the IRSatVideo-LEO [16]. As shown in Table IV, this study examines whether straightforward 2D-to-3D conversion can achieve satisfactory multi-frame detection performance. We also include 3D UNet variants with different base channels (denoted -B<sub>b</sub>) and our

TABLE II

CONFIGURATION AND EFFICIENCY OF FEEDBACK DESIGN VARIANTS. "PARAMS." REPRESENTS THE NUMBER OF PARAMETERS. FLOPs ARE CALCULATED BASED ON AN INPUT SEQUENCE SCALE OF  $5 \times 256 \times 256$ . THE ROW CORRESPONDING TO THE PROPOSED SPATIO-TEMPORAL SEMANTIC FEEDBACK FRAMEWORK IS HIGHLIGHTED WITH A GRAY BACKGROUND.

Function & Characteristic	Abbr.	Encoder	Decoder	Params $\downarrow$	FLOPs $\downarrow$
Decoder without semantic feedback	Dec-NoFB	[+, +, +, +, +]	[~, ~, ~, ~]	5.046M	26.979G
Encoder without semantic feedback	Enc-NoFB	[~, ~, ~, ~, ~]	[-, -, -, -]	2.748M	22.684G
All forward semantic feedback	All-Fwd	[+, +, +, +, +]	[+, +, +, +]	5.678M	30.144G
All backward semantic feedback	All-Bwd	[-, -, -, -, -]	[-, -, -, -]	5.678M	30.144G
Partial semantic feedback (Pattern 1)	Part-FB1	[+, ~, +, ~, +]	[-, ~, -, ~]	4.560M	26.559G
Partial semantic feedback (Pattern 2)	Part-FB2	[+, ~, +, ~, +]	[~, -, ~, -]	4.876M	25.343G
Full semantic feedback (Ours)	Full-FB	[+, +, +, +, +]	[-, -, -, -]	5.678M	30.144G

**Symbols:** +: FSTS-RM    ~: 3D Conv Block    -: BSTS-RM

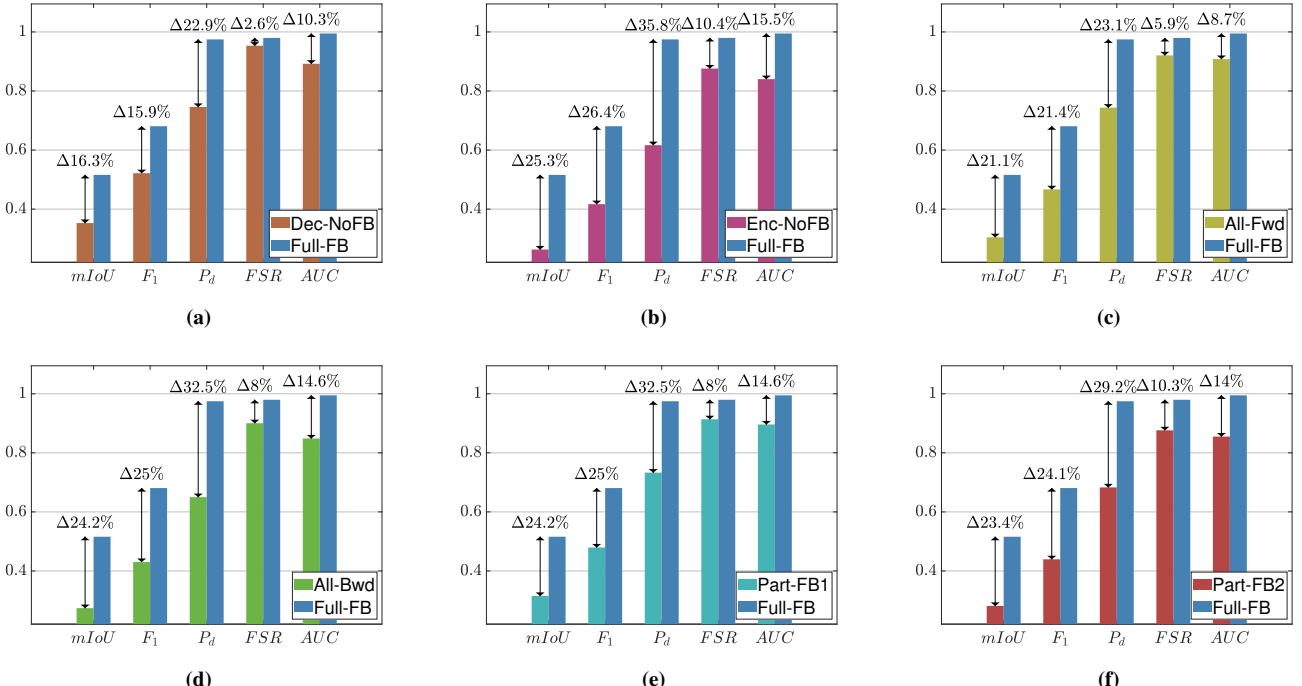


Fig. 5. Comparison of different feedback design variants against the Full-FB. Evaluation metrics include mean Intersection over  $mIoU$ ,  $F_1$ ,  $P_d$ ,  $FSR$ , and  $AUC$ , where  $\Delta$  represents the performance difference relative to the Full-FB. (a) Dec-NoFB vs Full-FB. (b) Enc-NoFB vs Full-FB. (c) All-Fwd vs Full-FB. (d) All-Bwd vs Full-FB. (e) Part-FB1 vs Full-FB. (f) Part-FB2 vs Full-FB.

TABLE III  
COMPARISON OF COMPUTATIONAL EFFICIENCY (FLOPs AND FPS) FOR VARYING SEQUENCE LENGTHS  $L$  AND SPARSE FRAME SAMPLING INTERVALS  $T$ . BOTH OF FLOPs AND FPS ARE CALCULATED BASED ON AN INPUT IMAGE SCALE OF  $256 \times 256$ .

$L$	$T = 1$		$T = 2$		$T = 3$		$T = 4$	
	FLOPs $\downarrow$	FPS $\uparrow$						
5	35.59G	8.4	30.14G	10.7	24.70G	14.2	19.25G	15.1
7	52.00G	8.0	46.56G	9.8	41.11G	11.2	35.67G	15.2
9	68.42G	7.5	62.97G	8.9	57.53G	10.5	52.08G	13.7
11	84.83G	7.6	79.39G	8.3	73.94G	8.9	68.50G	9.7
13	101.245G	7.4	95.80G	7.6	90.36G	9.1	84.91G	10.7
15	117.66G	7.7	112.214G	7.8	106.77G	8.9	101.32G	9.8

proposed FeedbackSTS-Det with two configurations (B8 and B16) for comprehensive comparison. Notably, 3D ACM and 3D UNet-B8 failed to converge during training (marked as  $\sim$ ) and are excluded from performance evaluation. Among all models, 3D UNet-B32 achieves the best detection performance ( $P_d$ : 92.56,  $AUC$ : 96.22) but requires substantial computational resources (24.32M parameters, 219.06G FLOPs). In contrast, our FeedbackSTS-Det-B8 delivers competitive performance ( $AUC$ : 95.53) with significantly lower complexity (5.68M parameters, 30.14G FLOPs) and achieves the lowest false alarm rate ( $F_a$ : 0.24).

In summary, compared to other 3D-modified frameworks, the 3D UNet [49] framework demonstrates the most stable overall performance. However, to fully leverage its capabilities, a large base channel number is necessary; otherwise, the

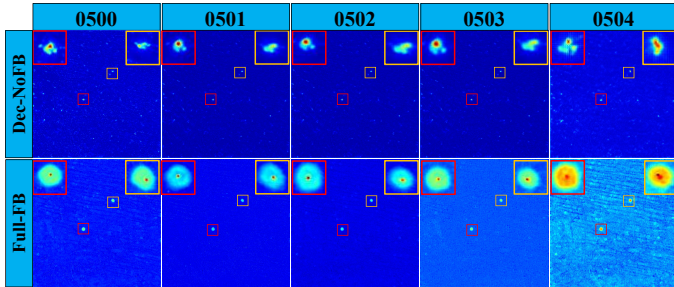


Fig. 6. Visual comparison of Dec-NoFB versus Full-FB using feature maps from the layer `dec_conv_1`, evaluated on frames 0500 ~ 0504 of sequence `EastAustralia1_09` in IRSatVideo-LEO dataset.

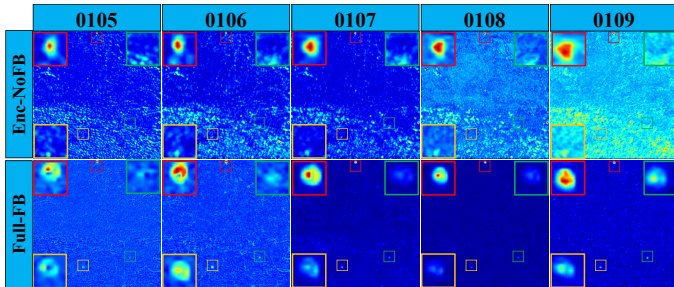


Fig. 7. Visual comparison of Enc-NoFB versus Full-FB using feature maps from the layer `conv_3`, evaluated on frames 0105 ~ 0109 of sequence `EastAustralia3_94` in IRSatVideo-LEO [16].

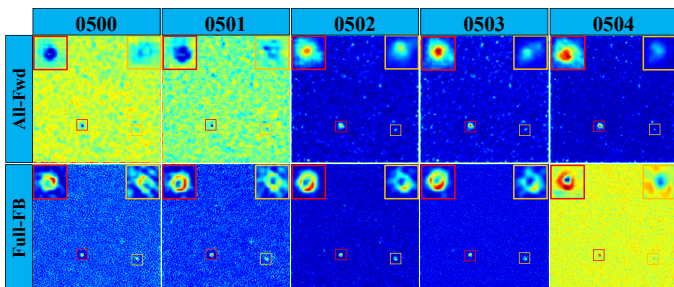


Fig. 8. Visual comparison of All-Fwd versus Full-FB using feature maps from the layer `dec_conv_3`, evaluated on frames 0500 ~ 0504 of sequence `EastAustralia5_07` in IRSatVideo-LEO [16].

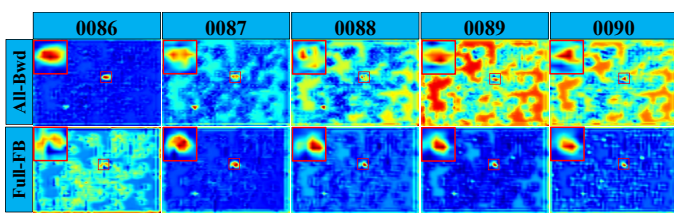


Fig. 9. Visual comparison of All-Bwd versus Full-FB using feature maps from the layer `conv_4`, evaluated on frames 0086 ~ 0090 of sequence 96 in NUDT-MIRSDT [42].

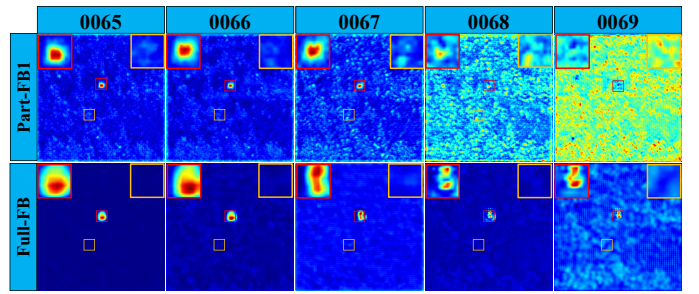


Fig. 10. Visual comparison of Part-FB1 versus Full-FB using feature maps from the layer `dec_conv_4`, evaluated on frames 0065 ~ 0069 of sequence `EastNorthAisa25_43` in IRSatVideo-LEO [16].

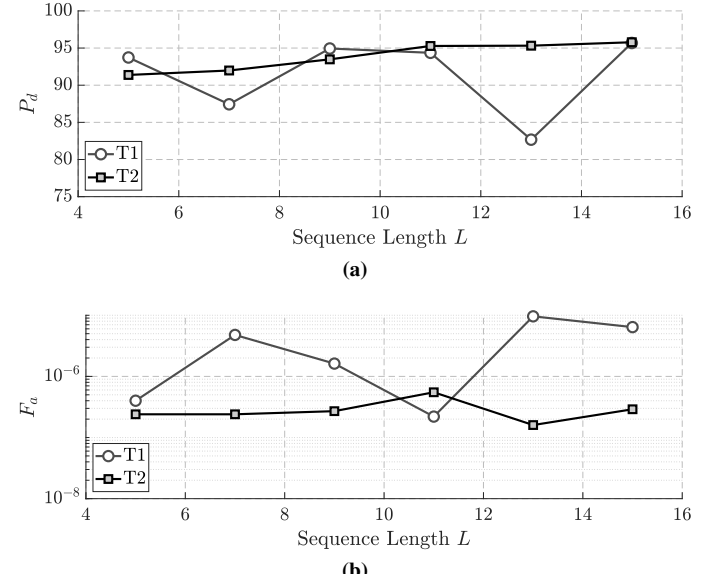


Fig. 11. Performance Metrics for the IRSatVideo-LEO [16] under no temporal sampling and T2 Conditions. (a)  $P_d$  vs.  $L$ . (b)  $F_a$  vs.  $L$ .

model may fail to effectively capture spatio-temporal features from multi-frame infrared sequences, leading to unsuccessful training. In contrast, with our proposed externally balanced and internally feature-iterative propagation framework, such a large base channel number is no longer required. Nevertheless, the notably lower  $P_d$  value of FeedbackSTS-Det-B16 compared to FeedbackSTS-Det-B8 indicates that simply increasing channel count does not guarantee better performance. This

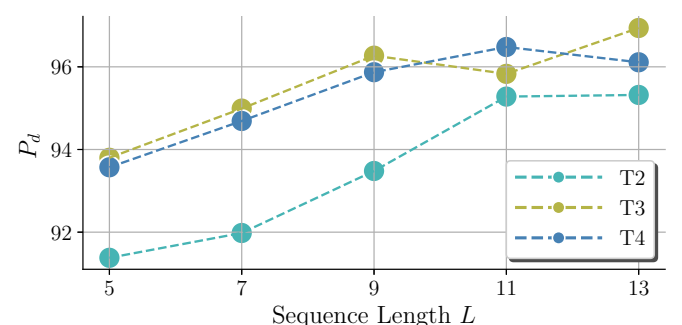


Fig. 12. Comparative Analysis of Sequence Length Effect on  $P_d$  under different sampling Intervals for the IRSatVideo-LEO [16].

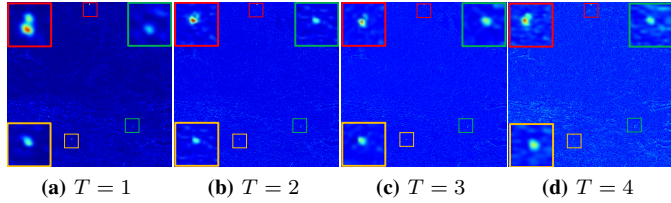


Fig. 13. Visual results of the FSTSIRM2 module outputs for frame 0106 of the sequence EastAustralia3\_94 from the IRSatVideo-LEO [16] under different sampling intervals. For clarity of observation, the targets are annotated with bounding boxes that are placed in the corners of the image. (a)  $T = 1$ . (b)  $T = 2$ . (c)  $T = 3$ . (d)  $T = 4$ .

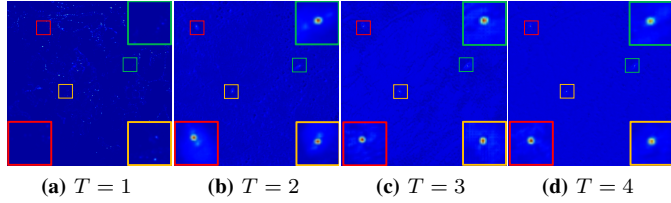


Fig. 14. Visual results of the BSTSRM1 module outputs for frame 0153 of the sequence EastNorthAsia0\_97 from the IRSatVideo-LEO [16] under different sampling intervals. For clarity of observation, the targets are annotated with bounding boxes that are placed in the corners of the image. (a)  $T = 1$ . (b)  $T = 2$ . (c)  $T = 3$ . (d)  $T = 4$ .

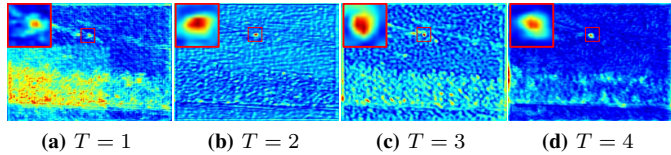


Fig. 15. Visual results of the BSTSRM3 module outputs for frame 0002 of the sequence92 from the NUDT-MIRSDT [42] under different sampling intervals. For clarity of observation, the targets are annotated with bounding boxes that are placed in the corners of the image. (a)  $T = 1$ . (b)  $T = 2$ . (c)  $T = 3$ . (d)  $T = 4$ .

TABLE IV

THE RESULTS OF  $P_d$  ( $\times 10^{-2}$ ),  $F_a$  ( $\times 10^{-6}$ ) AND  $AUC$  ( $\times 10^{-2}$ ) WERE ACHIEVED BY DIFFERENT 3D-MODIFIED FRAMEWORKS ON THE DATASET IRSATVIDEO-LEO[16]. THE 2D CONVOLUTIONS IN ACM [34], DNA-NET [52], AND UIU-NET [36] WERE MANUALLY REPLACED WITH 3D CONVOLUTIONS TO DERIVE THEIR CORRESPONDING 3D-MODIFIED FRAMEWORKS. FOR 3D UNET [49] AND OUR SELF-DESIGNED FEEDBACKSTS-DET, THE SUFFIX -B $b$  DENOTES THAT THE BASE CHANNEL NUMBER IS  $b$ . "PARAMS." REPRESENTS THE NUMBER OF PARAMETERS. FLOPs WERE CALCULATED BASED ON AN INPUT SEQUENCE SCALE OF  $5 \times 256 \times 256$ . THE ROWS CONTAINING OUR BENCHMARK MODELS FEEDBACKSTS-DET-B8 AND FEEDBACKSTS-DET-B16 ARE DISTINGUISHED WITH GRAY BACKGROUND HIGHLIGHTING.

Framework	Params $\downarrow$	FLOPs $\downarrow$	$P_d \uparrow$	$F_a \uparrow$	$AUC \uparrow$
3D ACM[34]	1.10M	5.25G	~	~	~
3D DNA-Net[52]	4.70M	70.29G	73.65	7.32	86.79
3D UIU-Net[36]	50.54M	272.13G	74.78	7.36	87.34
3D UNet[49]-B8	1.52M	13.81G	~	~	~
3D UNet[49]-B16	6.08M	54.92G	89.04	0.79	94.48
3D UNet[49]-B32	24.32M	219.06G	92.56	0.68	96.22
FeedbackSTS-Det-B8	5.68M	30.14G	91.38	0.24	95.53
FeedbackSTS-Det-B16	5.68M	105.43G	85.96	0.32	92.92

can be attributed to the limited number of sequences in commonly used multi-frame infrared small target datasets, which restricts sample diversity and makes the models prone to overfitting when an excessively large channel configuration is used. Considering the balance between performance and computational cost, we ultimately adopt FeedbackSTS-Det-B8 as our model.

## V. CONCLUSION

This paper presents a novel sparse frames-based spatio-temporal feedback network, i.e., STSFeedback Detector, for infrared small target detection. Its core is a closed-loop semantic feedback strategy with forward and backward refinement modules working jointly, enabling robust implicit registration and continuous spatio-temporal semantic refinement to suppress false alarms. Furthermore, an embedded sparse semantic module (SSM) performs structured sparse temporal modeling to capture long-range dependencies with low computational cost. Moreover, the overall procedure maintains a consistent training-inference pipeline, which ensures reliable performance transfer and increases model robustness. Ablation studies and superior results on multiple datasets confirm the effectiveness of FeedbackSTS-Det. The limitation of our work is that we only conduct experiments on a limited range of scenarios. Therefore, the model's robustness may be insufficient when dealing with extremely dim targets, strong clutter, or fast-moving objects, which could affect the generalizability of the results. In future work, we will optimize the network architecture and evaluate it on a more diverse range of infrared data scenarios, aiming to progressively improve the model's generalization capability.

## REFERENCES

- [1] Y. Zhang, Y. Zhang, R. Fu, Z. Shi, J. Zhang, D. Liu, and J. Du, "Learning nonlocal quadrature contrast for detection and recognition of infrared rotary-wing uav targets in complex background," *IEEE Transactions on Geoscience and Remote Sensing*, vol. 60, pp. 1–19, 2022.
- [2] X. Ying, Y. Wang, L. Wang, W. Sheng, L. Liu, Z. Lin, and S. Zhou, "Local motion and contrast priors driven deep network for infrared small target superresolution," *IEEE Journal of Selected Topics in Applied Earth Observations and Remote Sensing*, vol. 15, pp. 5480–5495, 2022.
- [3] M. Teutsch and W. Krüger, "Classification of small boats in infrared images for maritime surveillance," in *2010 international WaterSide security conference*. IEEE, 2010, pp. 1–7.
- [4] C. Hu, X. Dong, Y. Huang, L. Wang, L. Xu, T. Pu, and Z. Peng, "Smpisd-mtpnet: Scene semantic prior-assisted infrared ship detection using multi-task perception networks," *IEEE Transactions on Geoscience and Remote Sensing*, 2024.
- [5] V. Tramutoli, R. Corrado, C. Filizzola, N. Genzano, M. Lisi, N. Pergola *et al.*, "From visual comparison to robust satellite techniques: 30 years of thermal infrared satellite data analyses for the study of earthquake preparation phases," *Bollettino Di Geofisica Teorica e Applicata*, vol. 56, no. 2, pp. 167–202, 2015.
- [6] V. T. Tom, T. Peli, M. Leung, and J. E. Bondaryk, "Morphology-based algorithm for point target detection in infrared backgrounds," in *Signal and Data Processing of Small Targets 1993*, vol. 1954. SPIE, 1993, pp. 2–11.
- [7] M. M. Hadhoud and D. W. Thomas, "The two-dimensional adaptive lms (tdlms) algorithm," *IEEE transactions on circuits and systems*, vol. 35, no. 5, pp. 485–494, 1988.
- [8] C. Gao, D. Meng, Y. Yang, Y. Wang, X. Zhou, and A. G. Hauptmann, "Infrared patch-image model for small target detection in a single image," *IEEE transactions on image processing*, vol. 22, no. 12, pp. 4996–5009, 2013.

[9] Y. Dai and Y. Wu, "Reweighted infrared patch-tensor model with both nonlocal and local priors for single-frame small target detection," *IEEE journal of selected topics in applied earth observations and remote sensing*, vol. 10, no. 8, pp. 3752–3767, 2017.

[10] L. Zhang, L. Peng, T. Zhang, S. Cao, and Z. Peng, "Infrared small target detection via non-convex rank approximation minimization joint 1 2, 1 norm," *Remote Sensing*, vol. 10, no. 11, p. 1821, 2018.

[11] Y. Sun, J. Yang, and W. An, "Infrared dim and small target detection via multiple subspace learning and spatial-temporal patch-tensor model," *IEEE Transactions on Geoscience and Remote Sensing*, vol. 59, no. 5, pp. 3737–3752, 2020.

[12] G. Wang, B. Tao, X. Kong, and Z. Peng, "Infrared small target detection using nonoverlapping patch spatial-temporal tensor factorization with capped nuclear norm regularization," *IEEE Transactions on Geoscience and Remote Sensing*, vol. 60, pp. 1–17, 2021.

[13] T. Liu, J. Yang, B. Li, Y. Wang, and W. An, "Infrared small target detection via nonconvex tensor tucker decomposition with factor prior," *IEEE Transactions on Geoscience and Remote Sensing*, vol. 61, pp. 1–17, 2023.

[14] T. Ma, H. Wang, J. Liang, Y. Wang, J. Peng, Z. Kai, and X. Liu, "The temporal-spatial information fusion network for multi-frame infrared small target detection," *IEEE Transactions on Instrumentation and Measurement*, 2025.

[15] S. Zhuang, J. Peng, M. Qi, D. Wang, K. Li, and Y. Liu, "A temporal-semantic interaction network for multi-frame infrared small target detection," *Knowledge-Based Systems*, p. 113840, 2025.

[16] X. Ying, L. Liu, Z. Lin, Y. Shi, Y. Wang, R. Li, X. Cao, B. Li, S. Zhou, and W. An, "Infrared small target detection in satellite videos: a new dataset and a novel recurrent feature refinement framework," *IEEE Transactions on Geoscience and Remote Sensing*, 2025.

[17] D. Luo, Y. Xiang, H. Wang, L. Ji, S. Li, and M. Ye, "Deformable feature alignment and refinement for moving infrared small target detection," *Pattern Recognition*, vol. 169, p. 111894, 2026.

[18] Z. Shen, S. Chen, H. Wang, T. Zhang, X. Zhang, X. Xu, and X. Yang, "Low-level matters: An efficient hybrid architecture for robust multi-frame infrared small target detection," *arXiv preprint arXiv:2503.02220*, 2025.

[19] R. Cui, N. Li, J. Liu, and H. Zhao, "Mstcnet: Toward generalization improving for multi-frame infrared small target detection," *IEEE Journal of Selected Topics in Applied Earth Observations and Remote Sensing*, 2025.

[20] S. Kim and J. Lee, "Scale invariant small target detection by optimizing signal-to-clutter ratio in heterogeneous background for infrared search and track," *Pattern Recognition*, vol. 45, no. 1, pp. 393–406, 2012.

[21] C. P. Chen, H. Li, Y. Wei, T. Xia, and Y. Y. Tang, "A local contrast method for small infrared target detection," *IEEE transactions on geoscience and remote sensing*, vol. 52, no. 1, pp. 574–581, 2013.

[22] Y. Wei, X. You, and H. Li, "Multiscale patch-based contrast measure for small infrared target detection," *Pattern recognition*, vol. 58, pp. 216–226, 2016.

[23] Y. He, M. Li, J. Zhang, and Q. An, "Small infrared target detection based on low-rank and sparse representation," *Infrared Physics & Technology*, vol. 68, pp. 98–109, 2015.

[24] X. Wang, Z. Peng, D. Kong, and Y. He, "Infrared dim and small target detection based on stable multisubspace learning in heterogeneous scene," *IEEE Transactions on Geoscience and Remote Sensing*, vol. 55, no. 10, pp. 5481–5493, 2017.

[25] T. Zhang, Z. Peng, H. Wu, Y. He, C. Li, and C. Yang, "Infrared small target detection via self-regularized weighted sparse model," *Neurocomputing*, vol. 420, pp. 124–148, 2021.

[26] L. Zhang and Z. Peng, "Infrared small target detection based on partial sum of the tensor nuclear norm," *Remote Sensing*, vol. 11, no. 4, p. 382, 2019.

[27] X. Guan, L. Zhang, S. Huang, and Z. Peng, "Infrared small target detection via non-convex tensor rank surrogate joint local contrast energy," *Remote Sensing*, vol. 12, no. 9, p. 1520, 2020.

[28] X. Kong, C. Yang, S. Cao, C. Li, and Z. Peng, "Infrared small target detection via nonconvex tensor fibered rank approximation," *IEEE Transactions on Geoscience and Remote Sensing*, vol. 60, pp. 1–21, 2021.

[29] H.-K. Liu, L. Zhang, and H. Huang, "Small target detection in infrared videos based on spatio-temporal tensor model," *IEEE Transactions on Geoscience and Remote Sensing*, vol. 58, no. 12, pp. 8689–8700, 2020.

[30] T. Liu, J. Yang, B. Li, C. Xiao, Y. Sun, Y. Wang, and W. An, "Nonconvex tensor low-rank approximation for infrared small target detection," *IEEE Transactions on Geoscience and Remote Sensing*, vol. 60, pp. 1–18, 2021.

[31] T. Liu, J. Yang, B. Li, Y. Wang, and W. An, "Representative coefficient total variation for efficient infrared small target detection," *IEEE Transactions on Geoscience and Remote Sensing*, vol. 61, pp. 1–18, 2023.

[32] J. Li, P. Zhang, L. Zhang, and Z. Zhang, "Sparse regularization-based spatial-temporal twist tensor model for infrared small target detection," *IEEE Transactions on Geoscience and Remote Sensing*, vol. 61, pp. 1–17, 2023.

[33] F. Wu, H. Yu, A. Liu, J. Luo, and Z. Peng, "Infrared small target detection using spatiotemporal 4-d tensor train and ring unfolding," *IEEE transactions on geoscience and remote sensing*, vol. 61, pp. 1–22, 2023.

[34] Y. Dai, Y. Wu, F. Zhou, and K. Barnard, "Asymmetric contextual modulation for infrared small target detection," in *Proceedings of the IEEE/CVF winter conference on applications of computer vision*, 2021, pp. 950–959.

[35] T. Zhang, L. Li, S. Cao, T. Pu, and Z. Peng, "Attention-guided pyramid context networks for detecting infrared small target under complex background," *IEEE Transactions on Aerospace and Electronic Systems*, vol. 59, no. 4, pp. 4250–4261, 2023.

[36] X. Wu, D. Hong, and J. Chanussot, "Uiu-net: U-net in u-net for infrared small object detection," *IEEE Transactions on Image Processing*, vol. 32, pp. 364–376, 2022.

[37] M. Zhang, R. Zhang, Y. Yang, H. Bai, J. Zhang, and J. Guo, "Isnet: Shape matters for infrared small target detection," in *Proceedings of the IEEE/CVF conference on computer vision and pattern recognition*, 2022, pp. 877–886.

[38] H. Sun, J. Bai, F. Yang, and X. Bai, "Receptive-field and direction induced attention network for infrared dim small target detection with a large-scale dataset irdst," *IEEE Transactions on Geoscience and Remote Sensing*, vol. 61, pp. 1–13, 2023.

[39] S. Chen, L. Ji, S. Zhu, M. Ye, H. Ren, and Y. Sang, "Towards dense moving infrared small target detection: New datasets and baseline," *IEEE Transactions on Geoscience and Remote Sensing*, 2024.

[40] X. Liu, X. Li, L. Li, X. Su, and F. Chen, "Dim and small target detection in multi-frame sequence using bi-conv-lstm and 3d-conv structure," *Ieee Access*, vol. 9, pp. 135 845–135 855, 2021.

[41] J. Lin, C. Gan, and S. Han, "Tsm: Temporal shift module for efficient video understanding," in *Proceedings of the IEEE/CVF international conference on computer vision*, 2019, pp. 7083–7093.

[42] R. Li, W. An, C. Xiao, B. Li, Y. Wang, M. Li, and Y. Guo, "Direction-coded temporal u-shape module for multiframe infrared small target detection," *IEEE Transactions on Neural Networks and Learning Systems*, 2023.

[43] Y. Huang, X. Zhi, J. Hu, L. Yu, Q. Han, W. Chen, and W. Zhang, "Lmaformer: Local motion aware transformer for small moving infrared target detection," *IEEE Transactions on Geoscience and Remote Sensing*, 2024.

[44] F. Li, P. Rao, W. Sun, Y. Su, and X. Chen, "A low-signal-to-noise ratio infrared small-target detection network," *IEEE Journal of Selected Topics in Applied Earth Observations and Remote Sensing*, 2025.

[45] S. Zhu, L. Ji, J. Zhu, S. Chen, and W. Duan, "Tmp: Temporal motion perception with spatial auxiliary enhancement for moving infrared dim-small target detection," *Expert Systems with Applications*, vol. 255, p. 124731, 2024.

[46] J. Bian, S. Lin, D. Li, and X. Lu, "Statetrack: Infrared dim and small multi-target detection and tracking via state feature fusion," *Infrared Physics & Technology*, p. 105954, 2025.

[47] S. Peng, L. Ji, S. Chen, W. Duan, and S. Zhu, "Moving infrared dim and small target detection by mixed spatio-temporal encoding," *Engineering Applications of Artificial Intelligence*, vol. 144, p. 110100, 2025.

[48] K. He, X. Zhang, S. Ren, and J. Sun, "Deep residual learning for image recognition," in *Proceedings of the IEEE conference on computer vision and pattern recognition*, 2016, pp. 770–778.

[49] Ö. Çiçek, A. Abdulkadir, S. S. Lienkamp, T. Brox, and O. Ronneberger, "3d u-net: learning dense volumetric segmentation from sparse annotation," in *International conference on medical image computing and computer-assisted intervention*. Springer, 2016, pp. 424–432.

[50] J. Dai, H. Qi, Y. Xiong, Y. Li, G. Zhang, H. Hu, and Y. Wei, "Deformable convolutional networks," in *Proceedings of the IEEE international conference on computer vision*, 2017, pp. 764–773.

[51] Y. Huang, Z. Tang, D. Chen, K. Su, and C. Chen, "Batching soft iou for training semantic segmentation networks," *IEEE Signal Processing Letters*, vol. 27, pp. 66–70, 2019.

[52] B. Li, C. Xiao, L. Wang, Y. Wang, Z. Lin, M. Li, W. An, and Y. Guo, "Dense nested attention network for infrared small target detection," *IEEE Transactions on Image Processing*, vol. 32, pp. 1745–1758, 2022.

- [53] Y. Dai, Y. Wu, F. Zhou, and K. Barnard, "Attentional local contrast networks for infrared small target detection," *IEEE transactions on geoscience and remote sensing*, vol. 59, no. 11, pp. 9813–9824, 2021.
- [54] Q. Hou, L. Zhang, F. Tan, Y. Xi, H. Zheng, and N. Li, "Istdu-net: Infrared small-target detection u-net," *IEEE Geoscience and Remote Sensing Letters*, vol. 19, pp. 1–5, 2022.
- [55] F. Wu, T. Zhang, L. Li, Y. Huang, and Z. Peng, "Rpcanet: Deep unfolding rpca based infrared small target detection," in *Proceedings of the IEEE/CVF Winter Conference on Applications of Computer Vision*, 2024, pp. 4809–4818.
- [56] F. Wu, A. Liu, T. Zhang, L. Zhang, J. Luo, and Z. Peng, "Saliency at the helm: Steering infrared small target detection with learnable kernels," *IEEE Transactions on Geoscience and Remote Sensing*, 2024.
- [57] Y. Luo, X. Li, S. Chen, C. Xia, and L. Zhao, "Imnn-lwec: A novel infrared small target detection based on spatial-temporal tensor model," *IEEE Transactions on Geoscience and Remote Sensing*, vol. 60, pp. 1–22, 2022.

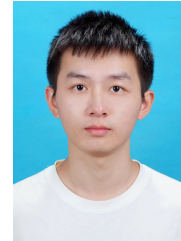
## VI. BIOGRAPHY SECTION



**Yian Huang** received the B.S. degree in communication engineering from Sun Yat-sen University (SYSU), Guangzhou, China, in 2022. He is currently pursuing the Ph.D. degree with the School of Information and Communication Engineering from University of Electronic Science and Technology of China (UESTC), Chengdu, China. His research interests include image processing, computer vision and infrared target recognition.



**Xiangyu Qiu** received his B.E. degree from the school of Information and Communication Engineering, University of Electronic Science and Technology of China, in 2024. He is pursuing an M.E. degree in School of Information and Communication Engineering, University of Electronic Science and Technology of China. His research interests include image processing, computer vision, and infrared small target detection.



**Liang Xu** received the B.E. degree in the School of Information and Communication Engineering from University of Electronic Science and Technology of China (UESTC), Chengdu, China, in 2024. He is currently pursuing the M.S. degree with the School of Information and Communication Engineering from UESTC, Chengdu, China. His research interests include image processing, computer vision and infrared target detection.



**Xian Zhang** received the B.S. degree in Information and Communication Engineering from University of Electronic Science and Technology of China (UESTC), Chengdu, China, in 2024. She is currently pursuing the M.S. degree with the School of Information and Communication Engineering, University of Electronic Science and Technology of China (UESTC), Chengdu, China. Her research interests include image processing and machine learning.



**Qing Qin** received her Ph.D. degree in arts from the Daejin University, Gyeonggi-do, Korea, in 2024. She is currently a lecturer with the Communication University of Zhejiang, Hangzhou. Her research interests include intelligent image production, digital video processing, and future advanced imaging.



**Zhenming Peng** (Senior Member, IEEE) received his Ph.D. degree in geodetection and information technology from the Chengdu University of Technology, Chengdu, China, in 2001. From 2001 to 2003, he was a Post-Doctoral Researcher with the Institute of Optics and Electronics, Chinese Academy of Sciences, Chengdu, China. He is currently a Professor with the University of Electronic Science and Technology of China, Chengdu. His research interests include image processing, machine learning, objects detection and remote sensing applications.



**Aji Mao** received the B.S. degree in electronic information engineering from China University of Mining and Technology (CUMT), Xuzhou, China, in 2021. He is currently pursuing the M.S. degree with the School of Information and Communication Engineering from University of Electronic Science and Technology of China (UESTC), Chengdu, China. His research interests include computer vision, large language model and infrared target recognition.